2026 IEEE International Conference on Robotics and Automation (ICRA 2026)
June 1-5, 2026. Vienna, Austria

Stroke-Based Variable-Damping with Force Attenuation for Capturing Large-Momentum Objects under Non-Zero Contact Velocity

Yang Chen[1], Junda Cao[2], Kai Gong[3], Yang Deng*[,1], Zhang Chen[1], Xudong Zheng[3], Zhili Hou[3] and Bin Liang[1]

***Abstract*— Basketball players catch fast passes, and porters unload goods without difficulty. These actions demonstrate how humans rely on intelligent regulation strategies to drive muscle activity. Replicating similar dynamic responses and strong impact absorption in robotics, however, remains a major challenge. Classical impedance control is theoretically sound and robust, but its fixed parameters require a trade-off between compliance and stability during high-impact interactions, which limits performance in dynamic scenarios. To address this issue, this paper proposes a Stroke-based Variable Damping Model (SVDM), which adjusts the damping coefficient adaptively according to the position error relative to the contact point. In addition, a Force Attenuation (FA) strategy is applied to the external forces injected into SVDM, resulting in the SVDM with Force Attenuation (FA-SVDM). Based on human biomechanical principles, we fabricated a 4-DOF robotic manipulator using 3D printing technology. Using FA-SVDM, the manipulator successfully captured a 1kg rigid sphere falling freely from 0.8m, resulting in a relative velocity upon contact of approximately 4 m/s. Under identical conditions, it exhibits superior performance compared to various fixed-damping configurations. We further developed a 6-DOF robotic manipulator equipped with a dexterous hand in the widely-used MuJoCo engine, employing quadratic programming (QP) for pre-contact trajectory tracking and FA-SVDM for post-contact energy dissipation, ultimately achieving human-like compliant capture of high-momentum flying objects using a single arm with a half-prehensile strategy.**

I. INTRODUCTION

Human proficiency in capturing high-momentum flying objects has drawn significant attention. Endowing robots with this capability can not only enhance operational efficiency in logistics applications [1], [2], [3], [4], but also provide safe capture solutions for space debris collection [5].

However, the complexity of robotic capture increases significantly when the target carries large momentum. The problem extends from simple trajectory interception to handling high-velocity impacts and post-contact energy dissipation (Fig. 1). The key challenge is to mitigate the initial impact force while dissipating the object's kinetic energy in a compliant yet stable manner. To address high-momentum impacts, variable impedance control methods have been proposed [6], typically by rapidly increasing stiffness and damping. However, for unknown targets, improper mass–stiffness–damping matching may induce oscillations or even instability, particularly in space applications.

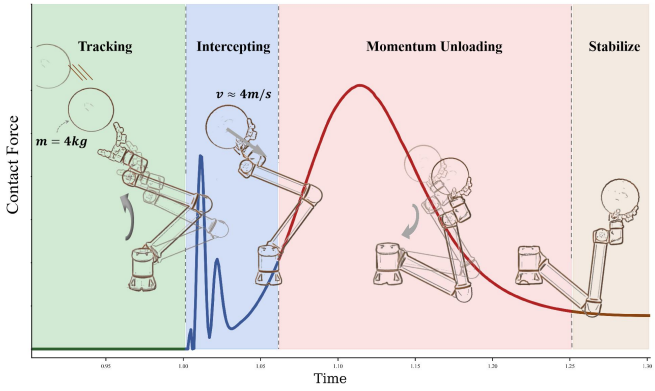

Fig. 1. A 6-degree-of-freedom robot manipulator equipped with a dexterous hand is employed to capture a large-momentum object weighing 4 kg, with relative velocity upon contact being approximately 4 m/s.

To address these limitations, we propose a Stroke-based Variable-Damping Model (SVDM), which adaptively regulates the damping coefficient according to the displacement relative to the contact point. A Force Attenuation (FA) mechanism is further introduced, forming the integrated FA-SVDM framework. This design enables high compliance during initial impact to mitigate contact forces, followed by increased damping for efficient energy dissipation.Beyond the adaptive strategy itself, we provide comprehensive stability analysis guaranteeing convergence to a stable equilibrium—an assurance often absent in heuristic or learning-based approaches. The proposed FA-SVDM specifically targets non-zero-velocity collisions and the associated post-impact energy dissipation in high-momentum capture tasks.

The overall capture framework is illustrated in Fig. 2 and validated through physical experiments and high-fidelity simulations. Comparative results demonstrate that FA-SVDM significantly outperforms fixed-damping configurations, achieving lower peak impact forces and shorter deceleration strokes under identical conditions. To further evaluate robustness, FA-SVDM is implemented in a challenging half-prehensile capture simulation, where a dexterous hand stabilizes the object without a fully enclosing grasp. This

This paper is supported by the National Natural Science Foundation of China under Grant 62573252.

* Yang Deng is the corresponding author.
[1] The Department of Automation, Tsinghua University, Beijing, 100084, China (email: yang-che23@mails.tsinghua.edu.cn; {dengyang, cz_da, bliang}@tsinghua.edu.cn).
[2] Xingjian College, Tsinghua University, Beijing, 100084, China (email: caojd22@mails.tsinghua.edu.cn).
[3] Qiyuan Lab, Beijing, 100194, China (email: buaa_gk@buaa.edu.cn; xudongzheng_buaa@163.com; hzl1334123@163.com).

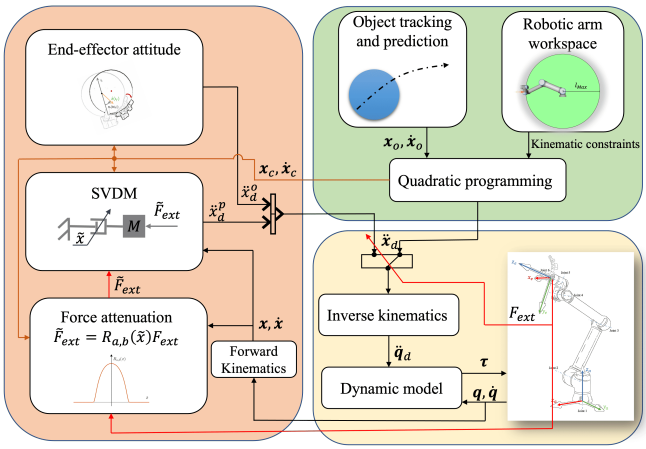

Fig. 2. Operational framework of the proposed capture system, where quadratic programming (QP) is employed for target tracking.

inherently less robust setting provides a stringent benchmark for controller performance.

The remainder of this paper is organized as follows: Section II reviews prior research related to this work. Section III presents the proposed approach in detail, including the design of the FA-SVDM, the stability analysis, and the digital implementation. Section IV reports and analyzes the experimental results on both the physical and simulation platforms. Finally, conclusions are drawn in Section V.

II. Related Work

Successful capture of flying objects depends on pre-contact tracking accuracy, impact handling, and post-contact energy dissipation. This section first introduces the impact model and its key parameters, then reviews methods from the perspectives of hard and soft catching, distinguished by whether explicit post-impact control strategies are employed.

A. Impact Model

In the pure torque control mode, the impact forces between the object and the robot is given by [7] :

$$\hat{F} = \frac{-(1+e)(\dot{\boldsymbol{x}} - \dot{\boldsymbol{x}}_o)^T \boldsymbol{u}}{\boldsymbol{u}^T(\boldsymbol{\Lambda}^{-1} + \frac{1}{m_o}\boldsymbol{I})\boldsymbol{u}}. \tag{1}$$

where $e \in (0,1)$ is the coefficient of restitution, $\dot{\boldsymbol{x}}, \dot{\boldsymbol{x}}_o \in \mathbb{R}^6$ denote the velocities of the robot and the object, respectively. $\boldsymbol{u}$ is the normal vector along the contact direction, m_0 is the mass of the object, and Λ is the inertia matrix of the robot.

The equivalent mass of the robot is defined as:

$$m_u(\boldsymbol{q}) = \left[\boldsymbol{u}^T \boldsymbol{\Lambda}_v^{-1} \boldsymbol{u}\right]^{-1} \tag{2}$$

where $\boldsymbol{\Lambda}_v \in \mathbb{R}^{3\times3}$ is the positional part of the decomposition of the inertia matrix $\boldsymbol{\Lambda}$.

From (1), impact force decreases with lower relative contact velocity. For instance, [8] reduced impact and rebound by replacing the target with a sandbag, thereby lowering the restitution coefficient e. The equivalent mass can likewise be reduced through lightweight robot design or redundancy-based kinematic configuration.

We next analyze existing methods for object capture under different robot configurations and target characteristics.

B. Hard catching approach

When the target is small and light, collision and energy dissipation can often be neglected. Hard catching methods focus on intercepting targets at predefined points using instantaneous stopping maneuvers [8], [9], [10], [11], [12], [13]. The main challenge is to compute the interception configuration—position and velocity—within a short time window and drive the robot to reach it accurately.

To address these challenges, several studies have proposed different strategies. [11] defined operational objectives in the image plane, generating 2D control schemes for target capture without explicit 3D reconstruction. Building on this, [12] developed a dual-layer motion planning algorithm for real-time trajectory generation, combined with a learning-based controller to improve joint tracking accuracy. For irregular objects, [13] employed offline-learned motion models for rapid online prediction of non-uniform targets, together with probabilistic methods to determine feasible grasp configurations. On integrated mobile platforms with manipulators and dexterous hands, [8] implemented a whole-body control strategy via two-phase reinforcement learning, enabling reliable capture of randomly thrown objects under dynamic conditions.

C. Soft Catching approach

The task becomes more complex when relative contact forces and object elasticity are considered [14], [15]. To address this, [16] achieved elastic ball capture using Model Predictive Control (MPC) combined with black-box gradient-aware optimization, incorporating velocity residuals into the catching-point configuration and introducing buffer strategies to mitigate rebound. Meanwhile, [17] modeled dynamical systems as Linear Parameter-Varying (LPV) systems, estimating parameters via Gaussian Mixture Models (GMMs) and developing a closed-loop optimal controller to maximize grasping softness under kinematic constraints.

When the target mass significantly increases, the task complexity not only arises from handling intricate collision dynamics but also from the need to compliantly dissipate the substantial kinetic energy of the target. To address this challenge, impedance control techniques have been widely applied for impact-aware catching [18], [19], [20], [7], [21]. Specifically, [20] proposed a hybrid optimization-learning framework that effectively absorbs post-impact forces through human demonstration-learned post-capture trajectories combined with variable stiffness control, enabling non-prehensile catching of objects at non-zero velocity. Their subsequent work [7] extended this approach to two-dimensional scenarios, but the captured targets remained relatively small compared to the robot's maximum actuation capabilities, and the method's effectiveness in full 3D captures remains unverified. As a pioneer in dynamic dual-arm capture of flying objects, [21] developed an integrated system combining motion estimation, prediction, contact selection, and stiffness modulation. The impact-aware motion planning strategy significantly reduces contact forces during robot-object interactions. Nevertheless, the system exhibits limitations,

including a restricted capture workspace, reaching the robot's joint limits, and underutilization of normal forces generated upon object contact, which together lower the upper bound of capture performance. Unlike the dual-arm setup in [21] or the fixed-parameter control in [20], our single-arm FA-SVDM efficiently avoids joint limits and reduces peak contact forces without extra hardware.

III. METHODOLOGY

This section details the FA-SVDM implementation. We first describe pure torque-mode impedance control, followed by the FA-SVDM design. Next, we present its stability proof and digital implementation. Finally, we discuss 6-DOF end-effector pose adjustment. Since strict VM realization is unnecessary for the well-studied pre-contact QP problem, we adopt a design similar to [12].

A. Impedance control

Typically, the dynamic modeling of a robot manipulator can be expressed as:

$$\boldsymbol{M}(\boldsymbol{q})\,\ddot{\boldsymbol{q}} + \boldsymbol{C}(\boldsymbol{q},\dot{\boldsymbol{q}}) + \boldsymbol{g}(\boldsymbol{q}) = \boldsymbol{\tau} + \boldsymbol{\tau}_{\text{ext}}. \tag{3}$$

where $\boldsymbol{q},\dot{\boldsymbol{q}},\ddot{\boldsymbol{q}} \in \mathbb{R}^n$ denote the joint positions, velocities, and accelerations, n is the number of DoFs, $\boldsymbol{M}(\boldsymbol{q}) \in \mathbb{R}^{n\times n}$ is the inertia matrix, $\boldsymbol{C}(\boldsymbol{q},\dot{\boldsymbol{q}}) \in \mathbb{R}^n$ is the Coriolis term, $\boldsymbol{g}(\boldsymbol{q}) \in \mathbb{R}^n$ is the gravity term, and $\boldsymbol{\tau} \in \mathbb{R}^n$ are the actuation torques, the transformation from the external force $\boldsymbol{F}_{\text{ext}}$ to the external torque $\boldsymbol{\tau}_{\text{ext}}$ is given by $\boldsymbol{\tau}_{\text{ext}} = \boldsymbol{J}(\boldsymbol{q})^\top \boldsymbol{F}_{\text{ext}}$.

The transformation from the joint space of the robot manipulator to the Cartesian space is given by:

$$\begin{cases} \dot{\boldsymbol{q}} = \boldsymbol{J}(\boldsymbol{q})^{-1}\,\dot{\boldsymbol{x}}, \\ \ddot{\boldsymbol{q}} = \boldsymbol{J}(\boldsymbol{q})^{-1}\Big(\ddot{\boldsymbol{x}} - \dot{\boldsymbol{J}}(\boldsymbol{q},\dot{\boldsymbol{q}})\,\boldsymbol{J}(\boldsymbol{q})^{-1}\,\dot{\boldsymbol{x}}\Big). \end{cases} \tag{4}$$

Substituting (4) into (3), we obtain:

$$\boldsymbol{\Lambda}(\boldsymbol{x})\,\ddot{\boldsymbol{x}} + \boldsymbol{\mu}(\boldsymbol{x},\dot{\boldsymbol{x}})\,\dot{\boldsymbol{x}} + \boldsymbol{J}(\boldsymbol{q})^{-\top}\boldsymbol{g}(\boldsymbol{q}) = \boldsymbol{J}(\boldsymbol{q})^{-\top}\boldsymbol{\tau} + \boldsymbol{F}_{\text{ext}}, \tag{5}$$

where

$$\begin{cases} \boldsymbol{\Lambda}(\boldsymbol{x}) = \boldsymbol{J}(\boldsymbol{q})^{-\top}\boldsymbol{M}(\boldsymbol{q})\boldsymbol{J}(\boldsymbol{q})^{-1}, \\ \boldsymbol{\mu}(\boldsymbol{x},\dot{\boldsymbol{x}}) = \boldsymbol{J}(\boldsymbol{q})^{-\top}\Big(\boldsymbol{C}(\boldsymbol{q},\dot{\boldsymbol{q}})\boldsymbol{J}(\boldsymbol{q})^{-1} \\ \qquad\qquad - \boldsymbol{M}(\boldsymbol{q})\boldsymbol{J}(\boldsymbol{q})^{-1}\dot{\boldsymbol{J}}(\boldsymbol{q},\dot{\boldsymbol{q}})\boldsymbol{J}(\boldsymbol{q})^{-1}\Big). \end{cases} \tag{6}$$

The essence of impedance control is the maintenance of a virtual dynamical model, usually formulated as a mass–spring–damper system:

$$\boldsymbol{\Lambda}_d\ddot{\tilde{\boldsymbol{x}}} + \boldsymbol{D}_d\dot{\tilde{\boldsymbol{x}}} + \boldsymbol{K}_d\tilde{\boldsymbol{x}} = \boldsymbol{F}_{\text{ext}}, \tag{7}$$

where $\tilde{\boldsymbol{x}} = \boldsymbol{x} - \boldsymbol{x}_d$ denotes the error between the EE's current position and its desired position. $\boldsymbol{\Lambda}_d$, $\boldsymbol{D}_d$, and $\boldsymbol{K}_d$ are the mass, damping, and stiffness matrices, respectively, which are typically designed as diagonal matrices.

The encoder provides $\boldsymbol{q}$ and $\dot{\boldsymbol{q}}$, from which $\boldsymbol{x}$ and $\dot{\boldsymbol{x}}$ can be computed, and the external force $\boldsymbol{F}_{\text{ext}}$ is measured by the force sensor. Substituting these data into (7) yields $\ddot{\boldsymbol{x}}$,which is then used in (5) to compute $\boldsymbol{\tau}$.

B. Design of the FA-SVDM

As mentioned in Section III-A, the parameter matrix in (7) is typically designed as a diagonal matrix, which decouples the system states. Therefore, analyzing the one-dimensional case is sufficient to achieve the same result, as also adopted in [23]. In 3D applications, decoupled Cartesian impedance control is used, where FA-SVDM modulates compliance along the impact normal (z-axis) and maintains high fixed stiffness and damping in the tangential directions (x, y) to avoid slippage.

The proposed FA-SVDM can be formulated as follows:

$$m\ddot{x}(t) + \mu\,|x(t)|^n\,\dot{x}(t) = R_{a,b}(x(t)) \cdot f_{\text{ext}}. \tag{8}$$

In (8), m denotes the virtual inertia, and $\ddot{x}(t)$, $\dot{x}(t)$, $x(t)$ represent the acceleration, velocity, and displacement of the controlled object, respectively. The controlled object is typically the EE, with the contact point taken as the origin. Here, μ is the damping coefficient, n is the exponential coefficient. f_{ext} represents the external force applied to the EE. $R_{a,b}(x(t))$ denotes the attenuation coefficient function, defined as follows:

$$R_{a,b}(x(t)) = \begin{cases} \kappa M^{-\frac{1}{(x(t)-a)(b-x(t))}}, & x(t) \in (a,b), \\ 0, & x(t) \in (-\infty,a] \cup [b,\infty). \end{cases}$$

The curve is illustrated in the following Fig. 3(a), where κ, M, a, and b are fixed parameters. Here, κ serves as the gain factor that ensures $R_{a,b}(x(t)) \in [0,1]$, while M influences the decay rate of the curve. Notably, $R_{a,b}(x(t))$ is a $\mathbf{C}^\infty$ function, which facilitates the subsequent stability analysis and provides a smooth transient performance.

For the damping term, let

$$D(\dot{x}(t),x(t)) = \mu\,|x(t)|^n\,\dot{x}(t).$$

To better observe the effect of $|x(t)|^n$, we set $\mu = 1$ and $\dot{x}(t) = 1$. The curve of $D(\dot{x}(t),x(t))$ with respect to $x(t)$ is shown in Fig. 3(b), during the initial phase of the contact, relatively low damping combined with a higher allocation of external force allows the EE to accelerate rapidly and achieve VM with the target object, without generating excessive contact forces. In the subsequent phase, as the damping increases and the external force progressively transfers to the actual dynamic system, where it is completely compensated, allowing the object's energy to be dissipated effectively.

Remind that larger values of n are not necessarily beneficial. An excessively large n can result in an ill-conditioned system, potentially causing oscillations.

Next, we discuss the passivity, stability, and digital implementation of (8). Before proceeding, we assume $f_{\text{ext}} > 0$, as capture tasks typically involve only a downward force between the object and the robot.

1) Passivity: For (8), define the system input as

$$u = R_{a,b}(x(t)) \cdot f_{\text{ext}},$$

and the system output as $\dot{x}$. To analyze its passivity, we construct the storage function $V(\dot{x}) = \frac{1}{2}m\dot{x}^2$, which yields:

$$\frac{d}{dt}(V(\dot{x})) = m\dot{x}\ddot{x} = -\mu\,|x|^n\,\dot{x}^2 + \dot{x}R_{a,b}(x(t))f_{\text{ext}} \tag{9}$$

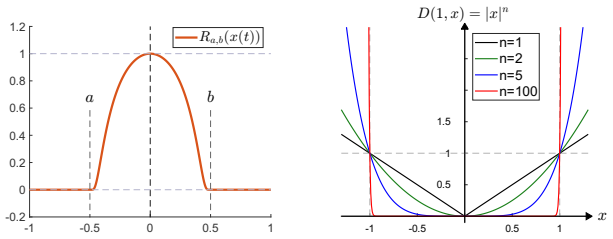

(a) (b)

Fig. 3. (a) Attenuation coefficient curve with $a = -0.5$ m, $b = 0.5$ m, $M = 1.2$, and $\kappa = 2.0736$; (b) Damping effect under different n.

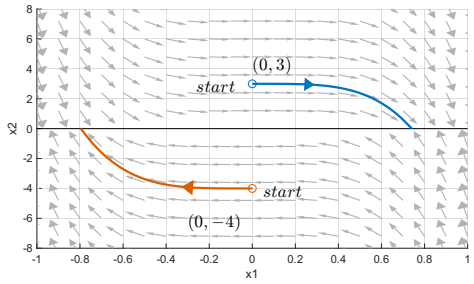

Fig. 4. The phase portraits of FA-SVDM in the free state($n = 3, m = 1, \mu = 40$).

it follows that:

$$u\dot{x} = R_{a,b}(x(t))f_{\text{ext}}\dot{x} = \dot{V}(\dot{x}) + \mu\left|x\right|^n\dot{x}^2 \tag{10}$$

Since $\mu\left|x\right|^n\dot{x}^2 \geq 0$, it follows that $u\dot{x} \geq \dot{V}(\dot{x})$, so, the system is passive. In the task considered in this paper, the system's passivity allows it to effectively dissipate the object's kinetic energy without storing additional energy.

2) Stability: For (8), define $x_1 \triangleq x(t)$ and $x_2 \triangleq \dot{x}(t)$. Its state-space representation is given by:

$$\begin{cases} \dot{x}_1 = x_2, \\ \dot{x}_2 = -\frac{\mu}{m}\left|x_1\right|^n x_2 + \frac{R_{a,b}(x_1)f_{\text{ext}}}{m}, \end{cases} \tag{11}$$

in the free state, the spatial velocity ratio R_{sv} is given by:

$$R_{sv} = \frac{\dot{x}_2}{\dot{x}_1} = -\frac{\mu}{m}\left|x_1\right|^n, \tag{12}$$

and the free-state phase portraits is shown in Fig. 4.

In the capture tasks, the initial value of $x_1(0)$ is set to 0. First, we consider the case where $x_2(0) \geq 0$, since $R_{a,b}(x_1)$ varies with the system state, in order to analyze the stability and steady-state properties of the system, we conduct the analysis in the following two stages:

a) $R_{a,b}(x_1) \neq 0$: we can get from (11)

$$\dot{x}_2 = \frac{1}{m}R_{a,b}(x_1)\cdot f_{\text{ext}} - \frac{\mu}{m}\left|x_1\right|^n x_2 \tag{13}$$

given that $x_2(0) \geq 0$,

$$-\frac{\mu}{m}\left|x_1\right|^n\dot{x}_1 \leq \dot{x}_2 \leq \frac{1}{m}f_{\text{ext}} \tag{14}$$

where, the left-hand side inequality defines its lower bound, while the right-hand side inequality defines its upper bound.

By analyzing $\dot{x}_{2\text{-UB}} = \frac{1}{m}f_{\text{ext}}$, we can obtain the phase plane equation:

$$x_{1\text{-UB}} = \frac{m}{2f_{\text{ext}}}\left(x_{2\text{-UB}}^2 - x_2(0)^2\right). \tag{15}$$

From Fig. 5(a), It can be observed that (15) intersects with $x_1 = b$ at $X_M = \left(b, \sqrt{\frac{2bf_{\text{ext}}}{m} + x_2(0)^2}\right)$, at the same time, $(x_{1\text{-LB}}, x_{2\text{-LB}})$ is generated from its phase portraits in the free-state. so we can observe that (13) is tightly constrained by the UB and LB curves. It is worth noting that although the LB curve may cross the x_1-axis when $x_1 < b$, trajectory (13) is prevented from reaching $x_2 = 0$ within the region $x_1 < b$ because $f_{\text{ext}} > 0$.

Therefore, in this stage, the system variables (x_1, x_2) do not exhibit finite escape.

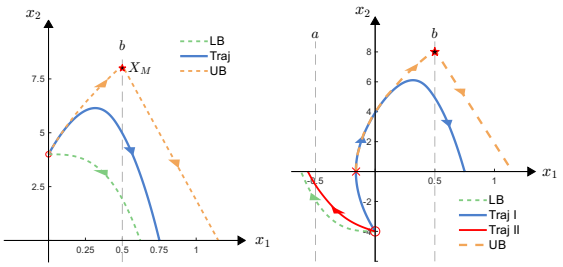

(a) (b)

Fig. 5. Phase trajectories with upper and lower bounds for initial velocities (a) $x_2(0) > 0$, (b) $x_2(0) < 0$.

b) $R_{a,b}(x_1) = 0$: Note that x_2 retains its sign after the end of the previous phase. Hence, we obtain:

$$m\dot{x}_2 = -\mu\left|x_1\right|^n x_2 \leq -\mu\left|b\right|^n x_2 \tag{16}$$

Hence, we obtain:

$$R_{\text{sv}} = \frac{\dot{x}_2}{\dot{x}_1} \leq -\frac{\mu}{m}\left|b\right|^n,$$

since the right-hand side of the inequality is constant, the phase trajectory will necessarily intersect with $x_2 = 0$, and system (16) is asymptotically stable by taking Lyapunov candidate function $V(x_2) = x_2^2$. Consequently, the trajectories of (11) will converge towards to a unique equilibrium point $(x_e, 0)$, which is the intersection obtained by using the geometric analysis mentioned above.

For the case $x_2(0) < 0$, Fig. 5(b) illustrates two possible scenarios. In the first case, as illustrated by Traj I, when the effect of the external force or damping is strong, x_2 first decreases to zero, after which the system behavior corresponds to Case III-B.2.a and Case III-B.2.b discussed earlier. In the second, as shown by Traj II, the trajectory crosses the boundary $x = a$ before x_2 decelerates to zero, eventually entering the case III-B.2.b discussed and converging to the equilibrium point.

In summary, the system is stable, and the equilibrium point exists and is unique.

3) Discretization constraint of FA-SVDM: When implementing (8) on a practical system, we do not expect the damping term to grow without bound, as this may lead to non-passivity and potential instability of the system. Therefore, we extend $\mu|x(t)|^n$ to $\mu\left|\frac{x(t)}{\sigma(x)}\right|^n$, by introducing $\sigma(x)$ as a dynamic scaling factor. Note that this modification does not affect the previous stability conclusions. Consequently, we

obtain the discrete-time implementation of (8), For notational simplicity, let $\tilde{f}_{\text{ext}}(k) = R_{a,b}(x(k-1))\, f_{\text{ext}}(k)$, it leads to

$$\begin{cases} \ddot{x}(k) = m^{-1}\left(\tilde{f}_{ext}(k) - \mu \left|\frac{x(k-1)}{\sigma(k-1)}\right|^n \dot{x}(k-1)\right), \\ \dot{x}(k) = \dot{x}(k-1) + \ddot{x}(k)\cdot \Delta T, \\ x(k) = x(k-1) + \dot{x}(k)\Delta T + \frac{1}{2}\ddot{x}(k)\Delta T^2. \end{cases} \tag{17}$$

Calculate the acceleration value at time $k+1$:

$$\ddot{x}(k+1) = m^{-1}\left(\tilde{f}_{\text{ext}}(k+1) - \mu \left|\frac{x(k)}{\sigma(k)}\right|^n \dot{x}(k)\right). \tag{18}$$

Let $\Delta U(k)$ denote the difference of the damping term:

$$\Delta U(k) = \mu \left|\frac{x(k)}{\sigma(x)}\right|^n \dot{x}(k) - \mu \left|\frac{x(k-1)}{\sigma(k-1)}\right|^n \dot{x}(k-1), \tag{19}$$

it follows that

$$\ddot{x}(k) - \ddot{x}(k+1) = m^{-1}\left(\tilde{f}_{\text{ext}}(k) - \tilde{f}_{\text{ext}}(k+1) + \Delta U(k)\right), \tag{20}$$

and

$$\begin{aligned} \mu \left|\frac{x(k)}{\sigma(k)}\right|^n \dot{x}(k) = &\frac{\mu}{|\sigma(k)|^n}\Big|x(k-1) + \dot{x}(k)\Delta T \\ &+ \frac{1}{2}\ddot{x}(k)\Delta T^2\Big|^n \big(\dot{x}(k-1) + \ddot{x}(k)\Delta T\big). \end{aligned} \tag{21}$$

Assume that $\sigma(k)$ varies relatively slowly as a tuning parameter, since in most cases it remains constant at 1. (19) can be approximated using the polynomial decomposition theorem as follows:

$$\begin{aligned} \Delta U(k) \approx &\frac{\mu}{|\sigma(k-1)|^n}\Big[|x(k-1)|^n \ddot{x}(k)\Delta T + n|x(k-1)|^{n-1} \\ &\cdot \big(\dot{x}(k)\Delta T + \tfrac{1}{2}\ddot{x}(k)\Delta T^2\big)\,\text{sign}\,\big(x(k-1)\big)\dot{x}(k-1)\Big]. \end{aligned} \tag{22}$$

By further transformation, we obtain

$$\begin{aligned} \Delta U(k) \approx \mu \left|\frac{x(k-1)}{\sigma(k-1)}\right|^n \Big[&\left(1 + n\frac{x(k-1) - x(k-2)}{x(k-1)}\right)\Delta T\, \ddot{x}(k) \\ &+ n\frac{x(k-1) - x(k-2)}{x(k-1)}\,\dot{x}(k)\Big]. \end{aligned} \tag{23}$$

In the analysis, the external force is assumed to be either zero or a constant value, the same assumption was also made in [23]. Thus, we have:

$$\ddot{x}(k) - \ddot{x}(k+1) = m^{-1}\Delta U(k). \tag{24}$$

Define

$$\alpha = \left\{1 - \frac{\mu}{m}\left|\frac{x(k-1)}{\sigma(k-1)}\right|^n \left(1 + n\frac{x(k-1) - x(k-2)}{x(k-1)}\right)\Delta T\right\}, \tag{25}$$

$$\beta = -n\frac{\mu}{m}\left|\frac{x(k-1)}{\sigma(k-1)}\right|^n \frac{x(k-1) - x(k-2)}{x(k-1)}, \tag{26}$$

the dynamics of (24) can be rewritten as the following equation:

$$\ddot{x}(k+1) = \alpha\ddot{x}(k) + \beta\dot{x}(k) \tag{27}$$

which is equivalent to the following state-space representation:

$$\begin{bmatrix}\dot{x}(k+1) \\ \ddot{x}(k+1)\end{bmatrix} = \begin{bmatrix}1 & \Delta T \\ \beta & \alpha\end{bmatrix}\begin{bmatrix}\dot{x}(k) \\ \ddot{x}(k)\end{bmatrix}. \tag{28}$$

For the matrix

$$A = \begin{bmatrix}1 & \Delta T \\ \beta & \alpha\end{bmatrix},$$

we compute its eigenvalues:

$$\det(\lambda I - A) = 0| \Longrightarrow (\lambda - 1)(\lambda - \alpha) - \beta\Delta T = 0. \tag{29}$$

For the case $\beta < 0$, the discrete-time system (27) is stable when $|\alpha| < 1$, which leads to the following inequality:

$$\frac{\mu}{m}\left|\frac{x(k-1)}{\sigma(k-1)}\right|^n \left(1 + n\frac{x(k-1) - x(k-2)}{x(k-1)}\right)\Delta T < 2, \tag{30}$$

then we can get:

$$\sigma(k-1) > \left\{\frac{1}{2m}\mu|x(k-1)|^n \left(1 + n\frac{x(k-1) - x(k-2)}{x(k-1)}\right)\Delta T\right\}^{\frac{1}{n}}. \tag{31}$$

Therefore, in the deployment on practical robotic systems, the selection rule for σ is as follows:

$$\begin{aligned} &\sigma(k-1) = \\ &\max\left(1, \left\{\frac{1}{2m}\mu|x(k-1)|^n \left(1 + n\frac{x(k-1) - x(k-2)}{x(k-1)}\right)\Delta T\right\}^{\frac{1}{n}}\right). \end{aligned} \tag{32}$$

From (32), when the sampling period ΔT is sufficiently small, σ will take the value 1 for the vast majority of the time, which will enventually fulfill the assumption mentioned below (21).

For the case of $\beta > 0$, (29) can be further analyzed, leading to conclusions similar to those of (31). However, since the task considered in this work does not involve $\beta > 0$, we do not elaborate on this case.

C. End-effector attitude control

In this work, we employ a half-prehensile strategy to capture the target sphere, allowing the object to slide on the EE. Unlike fully prehensile manipulation, where the object is rigidly secured by mechanical constraints, the dynamic nature of half-prehensile interaction imposes greater challenges on planning the EE's orientation. Importantly, once the object contacts the EE, visual occlusion prevents reliable estimation of the relative pose between the sphere and the EE using vision-based sensing. Consequently, monitoring the sphere's sliding on the EE must rely solely on proprioceptive feedback from the finger joints. To address this limitation, we propose a method to infer the relative position between the object and the EE based on finger angle measurements.

First, a PD torque control is applied to the finger joints:

$$u_i = k_{pi}\tilde{\beta}_i + k_{di}\dot{\tilde{\beta}}_i, \tag{33}$$

where u_i denotes the torque at each finger joint, $\tilde{\beta}_i = \beta_i - \beta_{id}$ represents the angular error of each finger joint, $\dot{\tilde{\beta}}_i$ denotes the angular velocity error, and k_{pi} and k_{di} are the PD parameters for each finger joint.

Thereafter, we design a desired trajectory for the EE's orientation. Taking the pitch angle as an example, the desired trajectory function is defined as follows:

$$\theta_b = \theta_0 e^{-\lambda_1 t} - \alpha_1, \tag{34}$$

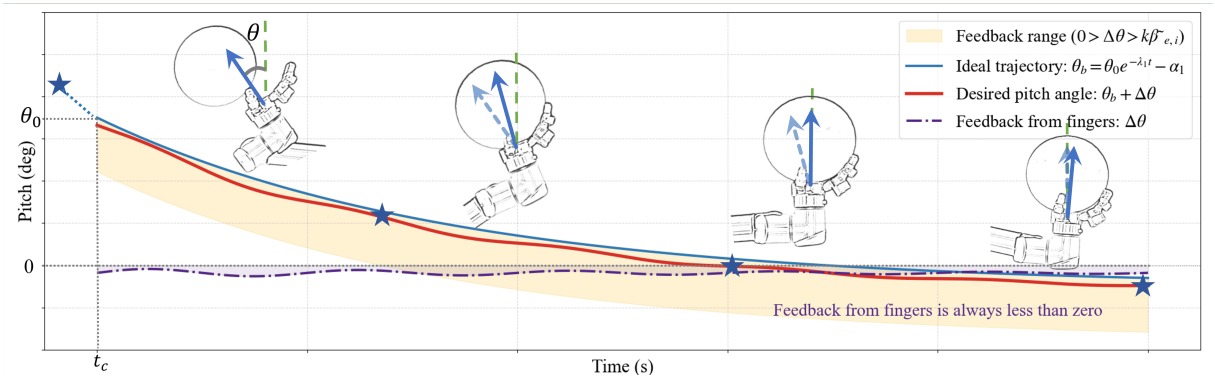

Fig. 6. End-effector attitude adjustment curve during momentum unloading.

where θ_0 denotes the EE's initial angle at the moment of interception, λ_1 is the exponential decay coefficient and α_1 represents the offset angle at stabilization. Next, finger feedback information is incorporated: $\Delta\theta = k\tilde{\beta}$, where $\tilde{\beta} = \frac{1}{9}\sum_{i=1}^{9}(\beta_i - \beta_{i,d})$, and k denotes the feedback coefficient.

Finally, the desired pitch angle is obtained as

$$\theta_d = \theta_b + \Delta\theta. \tag{35}$$

Moreover, for roll angle φ, we integrate the error feedback information from the thumb $\beta_{10,11,12}$, index finger $\beta_{1,2,3}$, and ring finger $\beta_{7,8,9}$:

$$\tilde{\beta}_\varphi = \frac{1}{3}\sum_{i=10}^{12}(\beta_i - \beta_{i,d}) + \frac{1}{3}\left(\sum_{i=1}^{3}(\beta_i - \beta_{i,d}) - \sum_{i=7}^{9}(\beta_i - \beta_{i,d}) - \beta_b\right), \tag{36}$$

where β_b is a fixed offset. (36) effectively prevents the ball from slipping between the thumb and index finger. Fig. 6 illustrates the attitude adjustment mechanism during energy dissipation. By combining the desired reference trajectory with proprioceptive feedback from the finger joints within a hybrid control framework, the target ball reaches dynamic equilibrium. Notably, the palm stabilizes in a slightly tilted configuration, improving the system's disturbance resistance.

IV. EXPERIMENTS AND RESULTS

In this section, we detail the experimental setup, including the physical platform and simulation environment, and analyze the results obtained under different damping configurations.

A. Experimental setup

To validate the advantages of FA-SVDM in non-zero velocity capture tasks, we constructed a 4-DOF robotic manipulator shown in Fig. 7(a). The motor layout was carefully designed to reduce inertia, and joints three and four are actuated via cable transmission. To eliminate the influence of other factors, such as relative impact velocity or visual tracking delays, the object was released from a fixed height to fall freely onto the stationary EE. Neither object tracking nor QP planning was utilized during this purely vertical drop validation.

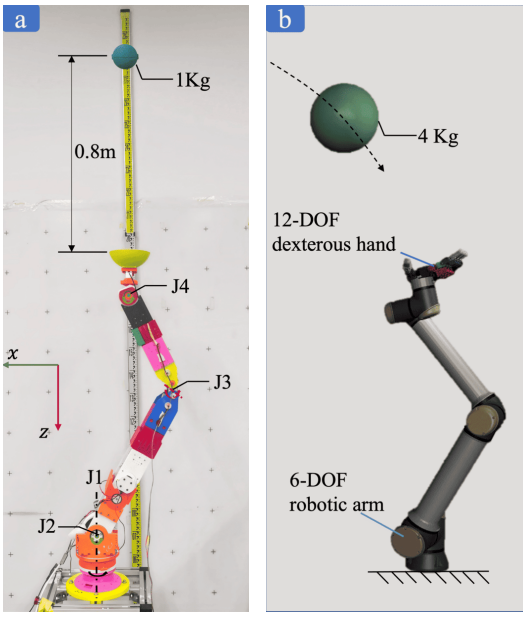

Fig. 7. Configuration of the proposed system: (a) physical experimental setup for validating FA-SVDM; (b) overview of the extended simulation-based experimental system.

We further conducted extended experiments in MuJoCo, building a 6-DOF robotic manipulator equipped with a 12-DOF dexterous hand, as illustrated in Fig. 7(b). The proposed FA-SVDM was employed to capture a larger-mass object in this platform.

B. Physical experiment

As mentioned in Section V-A, A rigid sphere with mass $m = 1$ kg was dropped freely from a height of $h = 0.8$ m, resulting in a relative velocity upon contact of approximately 4 m/s. The proposed FA-SVDM was employed to dissipate the post-contact energy, with model parameters set as $n = 2$, $m_x = 1$ kg, $m_z = 1$ kg, $\mu_x = 8000$, $\mu_z = 7000$, $\Delta T = 0.003$ s, $a = -0.3$ m, $b = 0.3$ m, $M = 1.2$, and $\kappa = 7.582$. The selection of these key parameters (e.g., bounds $a, b$and scaling factor M) is aligned with the robot's physical joint range limits and was optimized through offline simulations to ensure both compliance and kinematic safety.

For comparison, three additional fixed-damping settings

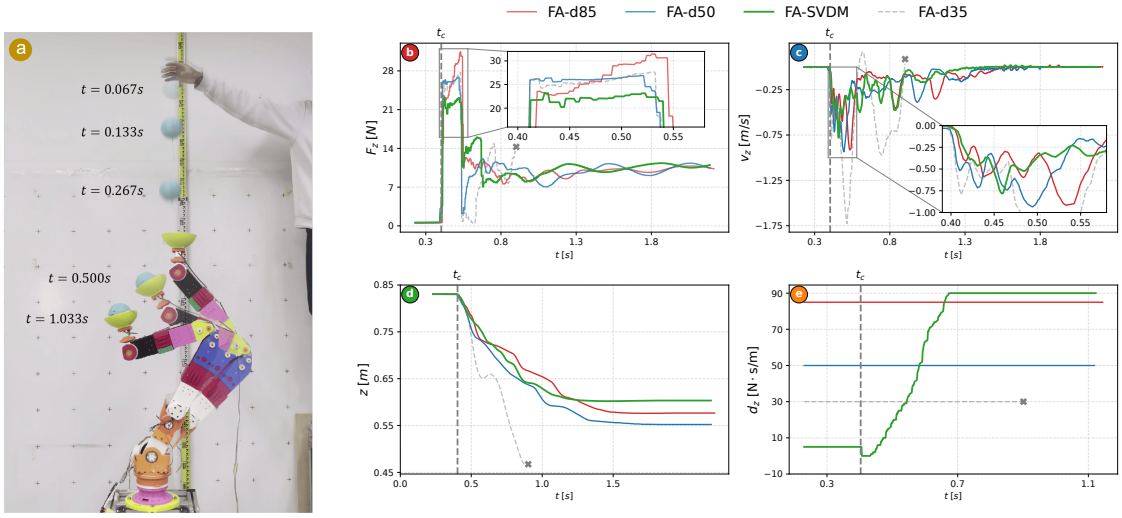

Fig. 8. Illustration of the physical experiments: (a) superimposed snapshots of the experimental process at multiple time steps; (b–e) plots of four damping settings, showing (b) contact force and (c) velocity in the z-direction, (d) displacement in the z-direction, and (e) variation of the damping coefficient.

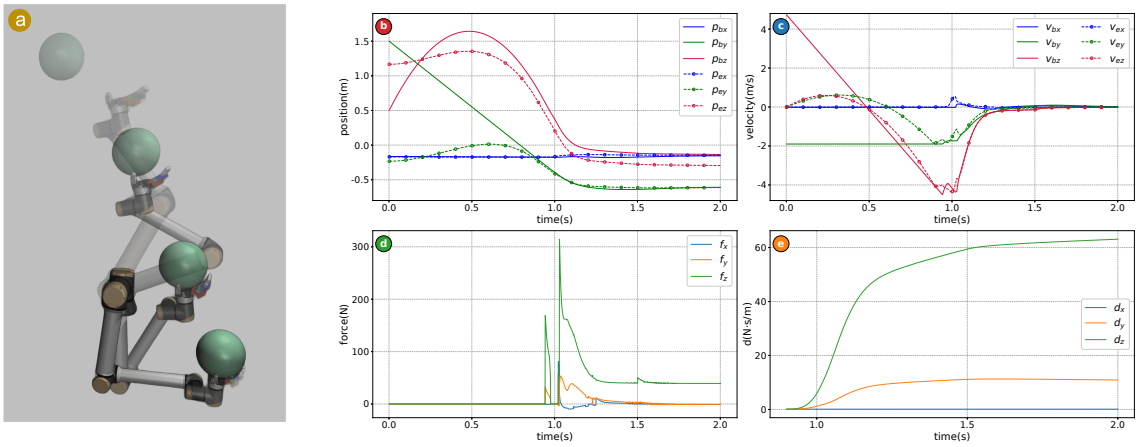

Fig. 9. Representative data from the extended simulation-based capture task: (a) superimposed snapshots at multiple time steps, b) position of ball and end-effector, c) velocity of ball and the EE, d) contact force of ball and end-effector, e) damping coefficient change.

($d = 30, 50, 85$ N · s/m) were tested. To confirm the consistency of the results, 4 repeated trials were conducted for each damping configuration, and representative results are shown in Fig. 8(b-e). The following metrics are defined to quantitatively evaluate the energy dissipation under different damping settings:

1) Maximum z-direction deceleration stroke, $\tilde{z}$;
2) The maximum contact force in the z direction, $F_{\max}$.

The analysis results are summarized in Table I.

As shown in Fig. 8(d), the group with $d = 35$, triggered joint limits, resulting in task failure. From the results in Table I, the group with $d = 85$ exhibited the highest $F_{\max}$, and the group with $d = 50$ had the longest deceleration stroke. In the pure torque control mode, the deceleration trajectory in Fig. 8(a) is not strictly vertical due to factors such as estimation errors in the dynamic model and joint friction. Nevertheless, this does not affect the conclusion that the proposed FA-SVDM achieves the smallest $F_{\max}$ and $\tilde{z}$, demonstrating its compliance and efficiency in handling non-zero velocity capture tasks.

TABLE I

INDICATORS AND RESULTS OF PHYSICAL EXPERIMENTS

	$\tilde{z}$ [m]	$F_{\max}$ [N]
$FA-d35$	$> 0.366^*$	27.74
$FA-d50$	0.278	26.88
$FA-d85$	0.254	31.46
FA SVDM	**0.227**	**22.16**

* The capture failed due to the end-effector triggering the joint kinematic limits at this stroke.

It should be noted that the task addressed in this paper is more challenging than the one in [20]. In the one-dimensional experiments of [20], The setup used $m = 0.5$ kg and $h = 0.27$ m, corresponding to 50% and 34% of the present experiment, respectively. The maximum contact force reported by their method was 23.6 N, which is higher than that achieved by the method proposed in this work.

C. Simulation extension experiment

Building on the previous experiments, we conducted extended simulations in MuJoCo [22], where the FA-SVDM parameters were set as follows : $\mu_x = 100$, $\mu_y = 200$, $\mu_z = 80$, $n = 3$, $m_x = m_y = m_z = 1$, $\Delta T = 0.001$ s, $a = -0.3$ m, $b = 0.3$ m, $M = 1.2$, and $\kappa = 7.5821$. As illustrated in Fig. 7(b), a spherical object with a radius of $r = 0.13$ m and mass 4 kg was selected as the capture target. During the tracking phase, the widely used QP method was employed to plan the motion of the manipulator. After contact, FA-SVDM was applied to dissipate the kinetic energy of the object in a compliant manner, while an end-effector orientation adjustment algorithm and joint-level PD control were used to stabilize the target. The results are shown in Fig. 9.

As seen in Fig. 9(c), a rebound occurs at the instant of contact due to the residual velocity, but the object's kinetic energy is quickly and smoothly dissipated thereafter. It is worth noting that the peak contact force in Fig. 9(d), when normalized by the object's weight (defined as $F_{\max}/(m_{\text{object}} \cdot g)$), is significantly larger than in the previous experiment. This discrepancy arises because contact force computation in MuJoCo relies on strict rigid-body collision models, whereas the real physical setup naturally mitigates initial impact forces due to its inherent mechanical flexibility and structural damping. The damping variation in Fig. 9(e) is consistent with the trends observed in the previous section.

Furthermore, in the attached video, more tests with different initial velocities illustrate that FA-SVDM handles the capture tasks effectively. A more comprehensive control framework incorporating null-space projection for secondary objectives (e.g., joint-limit avoidance and posture regulation) will be investigated in future work.

V. CONCLUSIONS

This paper addresses the challenge of robotic capture of high-momentum flying objects by proposing a novel variable impedance control framework, termed FA-SVDM. The core idea is to adaptively regulate the system damping coefficient based on the post-contact displacement of the end-effector, while dynamically attenuating the external force injected into the virtual dynamics. This enables high compliance during the initial collision phase and efficient energy dissipation in the subsequent stage. We provide a theoretical analysis of the controller's stability, ensuring system convergence.

The effectiveness of the FA-SVDM framework is validated through physical prototypes and high-fidelity simulations. Experimental results clearly demonstrate that, compared with various fixed-damping configurations and related methods, the proposed approach achieves both lower peak impact forces and shorter deceleration strokes in capture tasks, effectively resolving the trade-off between compliance and dissipation efficiency. This study offers a promising solution for efficient logistic manipulation in unstructured environments and the capture or de-spinning of high-Momentum space targets in orbital scenarios. Future work will focus on refining the physical system and performing comprehensive experimental validation.

REFERENCES

[1] Dehio, Niels, Yuquan Wang, and Abderrahmane Kheddar. "Dual-arm box grabbing with impact-aware MPC utilizing soft deformable end-effector pads." IEEE Robotics and Automation Letters 7.2 (2022): 5647-5654.

[2] Wang, Yuquan, et al. "Impact-aware task-space quadratic-programming control." The International Journal of Robotics Research 42.14 (2023): 1265-1282.

[3] Khurana, Harshit, and Aude Billard. "Motion planning and inertia-based control for impact aware manipulation." IEEE Transactions on Robotics 40 (2023): 2201-2216.

[4] van Steen, Jari, et al. "Impact-Aware Robotic Manipulation: Quantifying the Sim-To-Real Gap for Velocity Jumps." arXiv preprint arXiv:2411.06319 (2024).

[5] Abbott, Jake J. "Roboticists are grappling with space debris." Science Robotics 10.103 (2025): eadt5685.

[6] Kheddar, Abderrahmane, et al. "Editorial Introduction to the IEEE T-RO Special Collection on Impact-Aware Robotics." IEEE Transactions on Robotics 40 (2024): i-iv.

[7] Tassi, Francesco, et al. "IMA-catcher: An IMpact-aware nonprehensile catching framework based on combined optimization and learning." The International Journal of Robotics Research (2025): 02783649251345851.

[8] Zhang, Yuanhang, et al. "Catch it! learning to catch in flight with mobile dexterous hands." 2025 IEEE International Conference on Robotics and Automation (ICRA). IEEE, 2025.

[9] Lampariello, Roberto, et al. "Trajectory planning for optimal robot catching in real-time." 2011 IEEE International Conference on Robotics and Automation. IEEE, 2011.

[10] Bäuml, Berthold, Thomas Wimböck, and Gerd Hirzinger. "Kinematically optimal catching a flying ball with a hand-arm-system." 2010 IEEE/RSJ International Conference on Intelligent Robots and Systems. IEEE, 2010.

[11] Deguchi, Koichiro, Hironari Sakurai, and Shun Ushida. "A goal oriented just-in-time visual servoing for ball catching robot arm." 2008 IEEE/RSJ International conference on intelligent Robots and Systems. IEEE, 2008.

[12] Dong, Ke, et al. "Catch the ball: Accurate high-speed motions for mobile manipulators via inverse dynamics learning." 2020 IEEE/RSJ International Conference on Intelligent Robots and Systems (IROS). IEEE, 2020.

[13] Kim, Seungsu, Ashwini Shukla, and Aude Billard. "Catching objects in flight." IEEE Transactions on Robotics 30.5 (2014): 1049-1065.

[14] Dehio, Niels, and Abderrahmane Kheddar. "Robot-safe impacts with soft contacts based on learned deformations." 2021 IEEE International Conference on Robotics and Automation (ICRA). IEEE, 2021.

[15] Wang, Yuquan, et al. "Impact-aware task-space quadratic-programming control." The International Journal of Robotics Research 42.14 (2023): 1265-1282.

[16] Abeyruwan, Saminda, et al. "Agile catching with whole-body mpc and blackbox policy learning." Learning for Dynamics and Control Conference. PMLR, 2023.

[17] Salehian, Seyed Sina Mirrazavi, Mahdi Khoramshahi, and Aude Billard. "A dynamical system approach for softly catching a flying object: Theory and experiment." IEEE Transactions on Robotics 32.2 (2016): 462-471.

[18] Abiko, Satoko, Roberto Lampariello, and Gerd Hirzinger. "Impedance control for a free-floating robot in the grasping of a tumbling target with parameter uncertainty." 2006 IEEE/RSJ international conference on intelligent robots and systems. IEEE, 2006.

[19] Lampariello, Roberto, et al. "Tracking control for the grasping of a tumbling satellite with a free-floating robot." IEEE Robotics and Automation Letters 3.4 (2018): 3638-3645.

[20] Zhao, Jianzhuang, et al. "Impact-friendly object catching at non-zero velocity based on combined optimization and learning." 2023 IEEE/RSJ International Conference on Intelligent Robots and Systems (IROS). IEEE, 2023.

[21] Yan, Lei, et al. "Impact-aware bimanual catching of large-momentum objects." IEEE Transactions on Robotics (2024).

[22] Todorov, Emanuel, Tom Erez, and Yuval Tassa. "Mujoco: A physics engine for model-based control." 2012 IEEE/RSJ international conference on intelligent robots and systems. IEEE, 2012.

[23] Chen, Lu, et al. "Compliance while resisting: A shear-thickening fluid controller for physical human-robot interaction." The International Journal of Robotics Research 43.11 (2024): 1731-1769.